(For the sake of convenience, the references used in the supplementary section are listed at the end.)

Section 1. Illustration of mobile BLT-SARRP system

Our SARRP (Figure S1a) employs a dual focal X-ray source for irradiation (3 mm focal spot) and CBCT imaging (0.4 mm focal spot) (1,2). To achieve non-coplanar radiation delivery, it is equipped with a 360° isocentric gantry and a 4D (x, y, z translation and 360° rotation) robotic couch. For irradiation, 220 kVp X-ray beam ranging from 0.5 mm in diameter to 10 mm × 10 mm square field are available. A 20.5 cm × 20.5 cm amorphous silicon flat panel detector with 200 μm pixel pitch (Perkin-Elmer, Waltham, MA) is used to acquire 65 kVp X-ray projection image used for CBCT reconstruction. CBCT imaging is acquired by rotating the prone animal between the stationary X-ray source and detector panel.

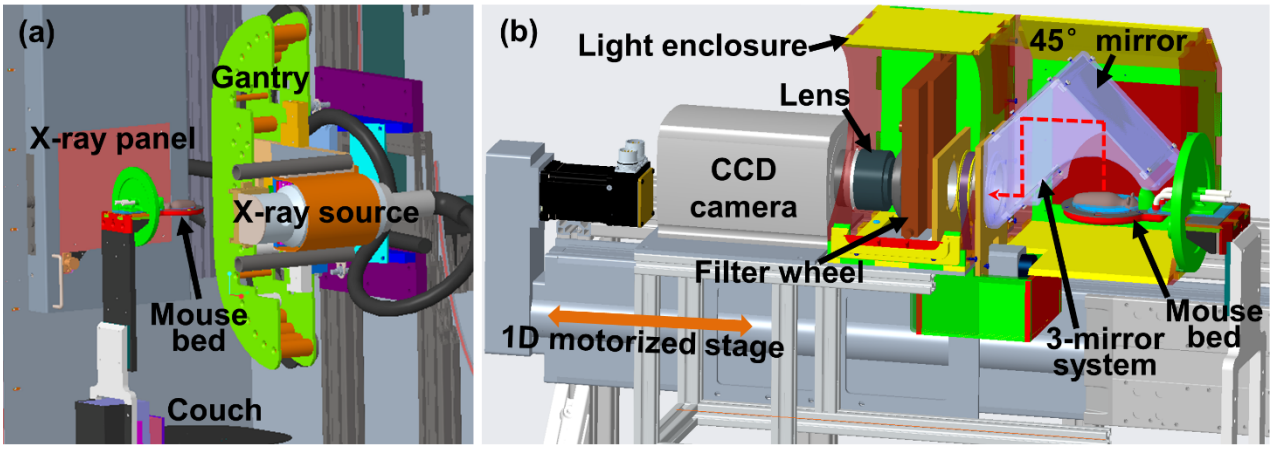

Figure S1. The schematic of (a) SARRP; (b) mobile BLT system; the optical signal emitted from mouse will be reflected by the three 45° mirrors to filter, lens and CCD camera. The 3-mirror system can rotate 180° around animal and capture multi-projection images. The mouse bed is transportable and it is compatible for both BLT and SARRP systems.

Our BLT system consists of a camera-filter-mirror optical assembly, a mobile cart and a transportable mouse bed (Figure S1b). For BL imaging, the entire optical assembly can be driven to the bed by a 1D linear stage (Parker 406XR, B.W.Rogers Co, Morgantown, PA). The optical assembly includes a CCD camera (iKon-L 936, Andor Technology, Belfast, UK), a 50-mm f/1.2 lens (Nikkor, Nikon Inc., Melville, NY), a filter wheel (Edmund Optcs Inc., Barrington, NJ), a 3-mirror system and a light-tight enclosure. The CCD camera has a 27.6 mm × 27.6 mm back-illuminated sensor at 13.5 μm/pixel, mounted with the lens for optical image acquisition. Four 20nm-FWHM band-pass filters (590-650 nm, 20 nm apart, transmission > 90%; Chroma Technology Corp., Bellows Falls, VT) mounted in the filter wheel enable multi-spectral BLI acquisition to improve BLT reconstruction accuracy (3,4). The 3-mirror (98% reflective, protected silver coating) system directs the bioluminescent signal emitted from the animal surface to the CCD, which can also rotate 180° around imaged object and capture multi-projection images. The optical path from our imaging plane through the mirrors to the front surface of the lens is 45 cm, and the imaging depth is 25 mm. The BLT system was operated in close proximity (within 2 m) to the SARRP to minimize animal transport. Because the SARRP CBCT is used to generate tetrahedral mesh of imaged animal for BLT reconstruction and define the coordinate for radiation, the 2D BLIs were mapped onto the

animal surface of the CBCT image and used as the input data for the optical reconstruction. Eight ball bearings were attached on the mouse bed to register the optical and CBCT coordinates (5). Studied animal is first imaged in the optical system to obtain surface BLIs, and then transferred to SARRP for CBCT imaging and BLT reconstruction, followed by BLT-guided irradiation. The optical imaging chamber was kept at 37 °C during BLI session. The animal was anesthetized and immobilized during the imaging and transport.

Section 2. Image segmentation to determine GBM volume in contrast CBCT/MRI

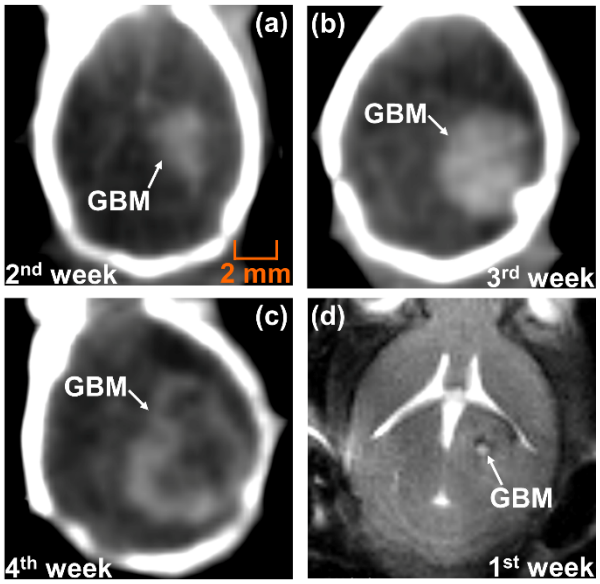

Figure S2. (a)-(c) Contrast CBCT labeled GBM at 2nd to 4th weeks after cell implanted and (d) T2-weighted MRI delineated GBMs for the 1st week case.

The *in vivo* procedures were carried out in accordance with the Johns Hopkins Animal Care and Use Committee. To establish the GBM model, 1.3×10^5 GL261-*Luc2* cells were stereotactically injected into mouse (C57BL/6J, female, 6-8 weeks old) left striatum (6). The contrast iodixanol agent 160 μL (Visipaque, 320 mgI/mL; GE Health Care, Chicago, IL) was administrated through retro-orbital injection 1 min before the contrast CBCT imaging acquired in our in-house high resolution CBCT system (7). The mouse brain images were cropped from the SARRP and contrast CBCT images, respectively. The cropped contrast CBCT image was registered to the SARRP CBCT image based on the skull rigid alignment in 3D Slicer (8-10) (Figure S2a-c). The registered contrast CBCT image in SARRP CBCT coordinate was then imported to MTALAB (MathWorks, Natick, MA) for segmentation. We first approximated the tumor location, based on the cell injected location (left hemisphere), and chose high and low thresholds to determine a range of CBCT values to segment the tumor. The high threshold, derived from the maximum value inside the tumor region, was used to remove the high density structure such as bone. The low threshold (CT_{low}) was chosen to determine the boundary between the tumor and normal tissue. We chose a $9 \times 9 \times 9$ voxel volume in right hemisphere (normal tissue region) and calculated the average CBCT value as the normal brain tissue CT value (CT_{brain}). To determine an appropriate CT_{low}, we calculated a series of $CT_{low} = R_{Threshold} \times CT_{brain}$, and $R_{Threshold}$ was empirically selected as 1.03-1.07 at 0.01 interval.

We visually examined through all the slices auto-segmented by these CT_{low} values and chose a suitable value which allows the segmented volume reasonably covering the contrast-labelled tumor area with minimum normal tissue region. After the step of the threshold segmentation, we manually remove any normal tissue regions which were selected but not within contrast-labeled region. For MRI image (Figure S2d) registration, the skull in MRI image was rigidly registered with that of SARRP CBCT image in 3D Slicer. The same segmentation process described above was applied to the MRI image, except the $R_{Threshold}$ was selected from 1.20-1.40 at 0.05 interval. Therefore, the segmented 3D GBM volume and the corresponding CoM can be established. We further investigated if contrast CBCT imaging and MRI may show significant difference in the GBM volume and CoM position. Second week GBM (n = 5) was chosen as an example for this study and a representative case is shown in Figure S3. The deviation between the CoMs and the volumes of contrast CBCT and MRI delineated GBM is 0.5 ± 0.1 mm and 1.2 ± 0.9 mm^3, respectively. This result suggested that the CoM and volume difference seen from the two imaging modalities unlikely introduce significant change to our end-results (Figures 1 and 3b in the main article).

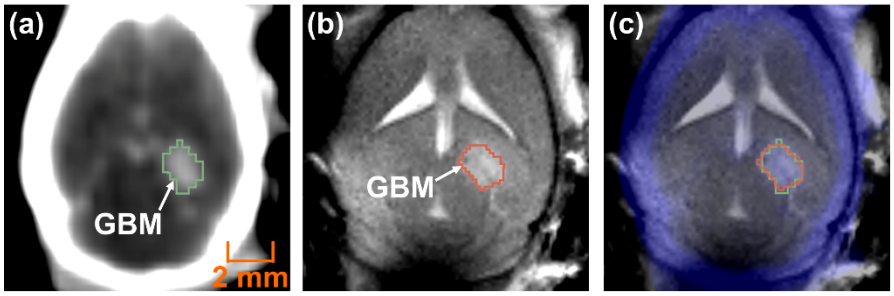

Figure S3. A representative result of segmented GBM volume from (a) contrast CBCT image and (b) T2-weighted MRI; (c) fused image of (a) and (b) shows the reasonable agreement of GBM localization and volume between contrast CBCT and MRI images.

Section 3. Optimization for mouse brain μ_a

To determine the optimal μ_a for reconstruction, we treated μ_a as the optimization parameter for our reconstruction process by minimizing the spatial difference between the CoMs retrieved from BLT and contrast CBCT/MRI. The detail steps are provided in the following.

Blood and water dominated the tissue absorption in the wavelength range considered in this work. In a simplified form, μ_a can be calculated as following (11):

$$\mu_a = \frac{\ln(10)\,BC_{m,HGb}}{MW}\left(S\varepsilon_{HbO_2} + (1-S)\varepsilon_{Hb}\right) + W\mu_{a,water} \quad (1)$$

where S is the oxygen saturation of hemoglobin (HGb), as $S = C_{HbO_2}/\left(C_{HbO_2} + C_{Hb}\right)$, C_{HbO2}, ε_{HbO2} are the oxygenated HGb concentration and extinction coefficient respectively, and C_{Hb}, ε_{Hb} are the quantities for the case of deoxygenated HGb. $C_{HGb} = C_{HbO2} + C_{Hb}$ is the total HGb concentration. B and W are the blood and water volume fractions in tissue respectively. $C_{m,HGb}$ is HGb mass concentration within blood. MW is molecular weight of HGb. $\mu_{a,water}$ is water absorption coefficient. $C_{m,HGb}$ = 150 $g{\cdot}L^{-1}$ and MW = 64,458 $g{\cdot}mol^{-1}$ were used in our calculation.

Table 1. Parameters for *in vivo* brain (11)

Tissue	C_{HGb} (μM)	B (%)	S (%)	W (%)
Neonatal brain (12)	39.7	1.71	58.7	NA
Neonatal brain (13)	64.7	2.78	70.0	NA
Rat brain cortex (14)	87.3	3.75	60.7	NA
Rat brain cortex (15)	71.0	3.05	59.0	NA
Mouse Brain (16)	174	7.48	68.4	31

Table 2. Extinction coefficient (17) and water absorption coefficients (18)

λ (nm)	ε_{HbO2} (mm^{-1} M^{-1})	ε_{Hb} (mm^{-1} M^{-1})	$\mu_{a,water}$ (mm^{-1})
590	1440.1	2832.4	1.35×10^{-4}
610	150.6	944.4	2.64×10^{-4}
630	61.0	514.9	2.92×10^{-4}
650	36.8	375.0	3.40×10^{-4}

Equation (1) was used to calculate the brain μ_a using the values from Table 1 and 2. In Table 1, the W values for the species we considered are not always available, except that Reference (16) provides the value of mouse brain as 31%. Due to the limit data availability, we investigated if there is significant contribution of water to μ_a for the cases we considered in Table 1. We defined the contribution of water to μ_a as P, and $P = \frac{W\mu_{a,water}}{\mu_a} = \frac{W\mu_{a,water}}{B\mu_{a,blood} + W\mu_{a,water}}$, where $\mu_{a,blood} = \frac{\ln(10)C_{m,HGb}}{MW}\left(S\varepsilon_{HbO_2} + (1-S)\varepsilon_{Hb}\right)$ is the absorption coefficient of blood in brain. By assuming water is the dominating component in light absorption beside the blood, we can write $W = 1 - B$ and P as $P_{max} = \frac{(1-B)\mu_{a,water}}{B\mu_{a,blood} + (1-B)\mu_{a,water}}$. The P_{max} in different brain tissues at 590, 610, 630 and 650 nm can be calculated and listed in Table 3. The largest value of P_{max} is 2.02%, and the corresponding contribution of HGb to μ_a is 97.98%. Therefore, for the wavelength we considered, the contribution of water to μ_a is insignificant compared to that of HGb. We then used 31% (Table 1) as the estimated value of W in Equation (1) for all the cases we considered. The Table 3 shows calculated P_{max} and μ_a.

Table 3. μ_a and P_{max} calculated from B, $\mu_{a,blood}$, $\mu_{a,water}$ for various brain tissues

Tissue (reference)	λ (nm)	B (%)	$\mu_{a,blood}$ (mm^{-1})	$\mu_{a,water}$ (mm^{-1})	P_{max} (%)	μ_a (mm^{-1})
Neonatal brain (12)	590	1.71	10.80	1.35×10^{-4}	0.07	0.1847
	610	1.71	2.56	2.64×10^{-4}	0.59	0.0439
	630	1.71	1.33	2.92×10^{-4}	1.24	0.0229
	650	1.71	0.95	3.40×10^{-4}	2.02	0.0163
Neonatal brain (13)	590	2.78	9.96	1.35×10^{-4}	0.05	0.2768
	610	2.78	2.08	2.64×10^{-4}	0.44	0.0580
	630	2.78	1.06	2.92×10^{-4}	0.96	0.0295
	650	2.78	0.74	3.40×10^{-4}	1.58	0.0207
Rat brain cortex (14)	590	3.75	10.65	1.35×10^{-4}	0.03	0.3994
	610	3.75	2.48	2.64×10^{-4}	0.27	0.0930
	630	3.75	1.28	2.92×10^{-4}	0.58	0.0482
	650	3.75	0.91	3.40×10^{-4}	0.95	0.0342
Rat brain cortex (15)	590	3.05	10.78	1.35×10^{-4}	0.04	0.3287
	610	3.05	2.55	2.64×10^{-4}	0.33	0.0779
	630	3.05	1.32	2.92×10^{-4}	0.69	0.0405
	650	3.05	0.94	3.40×10^{-4}	1.14	0.0288
Mouse Brain (16)	590	7.48	10.07	1.35×10^{-4}	0.02	0.7533
	610	7.48	2.15	2.64×10^{-4}	0.15	0.1609
	630	7.48	1.10	2.92×10^{-4}	0.33	0.0820
	650	7.48	0.77	3.40×10^{-4}	0.54	0.0577

From Table 3, the ranges of μ_a among all the brain tissues we considered are:

$\mu_{a,590} \in [0.1847, 0.7533]$ mm^{-1}; $\mu_{a,610} \in [0.0439, 0.1609]$ mm^{-1};

$\mu_{a,630} \in [0.0229, 0.0820]$ mm^{-1}; $\mu_{a,650} \in [0.0163, 0.0577]$ mm^{-1}.

From Equation (1), μ_a is the function of B, S and W. Because the contribution of water to brain μ_a is insignificant compared to that of HGb, we can assume μ_a mostly depend on B and S and adjust these two parameters to retrieve the μ_a within the aforementioned ranges. For S, we chose the value in between 0 and 1 at 0.2 interval. Figure S4 shows the searching ranges of B and S (gray area) at 590, 610, 630, and 650 nm. The upper and lower bound of μ_a for each wavelength is labeled by the dash lines in the subfigure of Figure S4. For a given value of S, we can find a group of corresponding B values at each wavelength. We further derived the range of B from 590 to 650 nm by choosing the overlapped B values among all the wavelength cases at a given S value. The final range of B for a given S within the upper and lower bound of μ_a are:

$B_{S=0} \in [0.0122, 0.0287]$; $B_{S=0.2} \in [0.0135, 0.0350]$; $B_{S=0.4} \in [0.0151, 0.0449]$;

$B_{S=0.6} \in [0.0177, 0.0626]$; $B_{S=0.8} \in [0.0291, 0.0818]$; $B_{S=1} \in [0.0826, 0.0976]$.

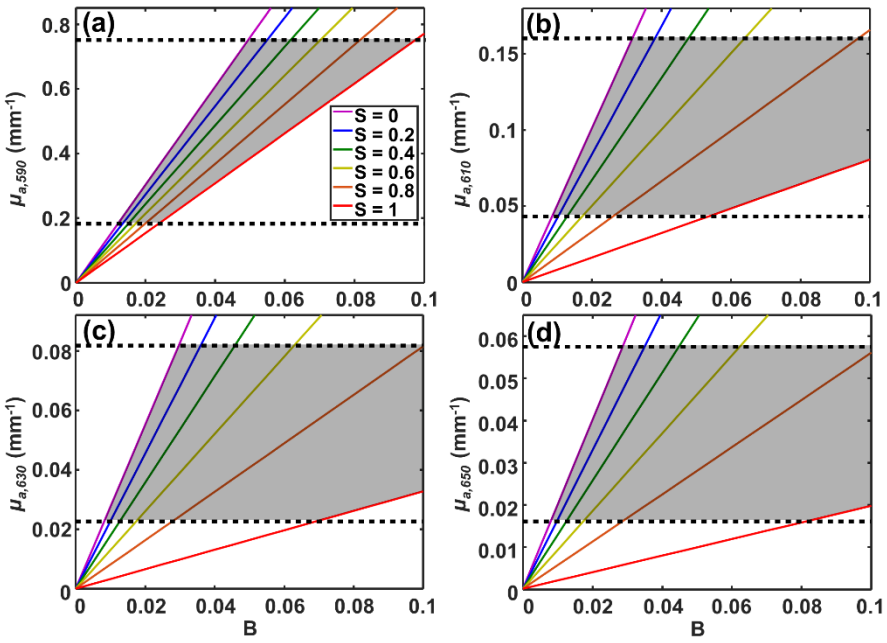

Figure S4. Ranges (gray area) of B and S at (a) 590, (b) 610, (c) 630 and (d) 650 nm within the upper and lower bound (dash lines) of μ_a.

A series of μ_a from 590 to 650 nm were derived based on the B and S set described above, and were entered into our BLT reconstruction engine. The resulted CoMs were compared to the CoMs of the contrast-CBCT/MRI-delineated GBM volume. For mesh generation, we utilized NIRFAST (19,20) to generate meshes subject to mesh-generation parameters (shown below). These parameters were used to provide a range of the size and shape of tetrahedral elements. It renders that even we used the same parameters for each mesh generation, the detail of the resulted mesh can be different. Moreover, our reconstruction algorithm, incomplete variables truncated conjugate gradient method with permissible region-shrinking strategy, is sensitive to the detail of the mesh. To reduce the influence of the numerical

mesh on the BLT reconstruction, for a given animal, we generated three meshes. The sets with the CoM deviation < 1 mm among the three meshes were selected and averaged as the optimal set of μ_a for a given animal. The same approach was applied to five GBM-bearing mice at the same tumor age. The averaged μ_a of the five studied animals was taken as the final set for GBM-bearing mice at a given tumor age.

The mesh-generation parameters are listed below:

1) Lower bound for the angles of surface mesh facets: 30°;
2) Upper bound for the distances between facet circumcenters and the centers of their surface Delaunay balls: 1 mm;
3) Upper bound for the radii of surface Delaunay balls: 0.7 mm;
4) Upper bound for the circumradii of mesh tetrahedral elements: 0.76 mm;
5) Upper bound for the radius-edge ratio of mesh tetrahedral elements: 1.

Section 4. Treatment planning

MuriPlan (Xstrahl Inc., Suwanee, GA), treatment planning system for SARRP, was used to design the radiation plan, based on the ETV centered at BLT-reconstructed CoM. The combination of SARRP gantry and couch (0-150° with 30° spacing) with 5 × 5 mm^2 square collimator was used to generate the non-coplanar 6-arc delivery (Figure S5a) which led to a nearly spherical dose distribution to cover the ETV. To avoid the collision between the mouse bed and gantry, for the couch at 60°, 90°, and 120°, we applied gantry angle from -90° to 30°, and for the couch at 0°, 30°, and 150°, we used gantry angle from -90° to 90°.

Figure S5b shows average DVH with STD (n = 5, 2nd-week GBM bearing mice) for ETV. As we expected, due to the fixed target volume, ETV, and the X-ray homogenous environment in brain tissue, the DVH deviation is ≤ 3.1%. It renders that we can apply same treatment plan for GBM-bearing mice under a well-controlled experiment environment *i.e.* consistent tumor size, location, and animal size. Our planning goal is 95% of the prescribed dose (15 Gy) covering 95% of ETV. To satisfy this criterion and minimize normal tissue toxicity, we prescribed 15 Gy at 84% isodose line, which resulted in 95% of the prescribed dose (14.25 Gy at 80% isodose line shown in Figure S5b) covering 94.9 ± 0.1% of ETV for all the mice considered. Figure S5c-d show DVHs with STD for the 6-arc conformal and single-(dorsal-to-ventral) DV-beam irradiation for contrast-labeled GBM and normal tissue. A clear underdose for the contrast GBM is shown in the DVH in the single field irradiation compared to the arc conformal delivery (Figure S5d vs. c). It is worthwhile to mention that for the single field irradiation demonstrated in this study, it can be an ideal scenario compared that to other tumor models, because the cell implementation site is known and the size of tumor is relatively small (2nd week-old GBM compared that to the later week (Figure 1 in the main article)). It indicates that for other tumor model or large tumor, single field irradiation may produce even more inferior coverage than those shown in Figure S5d.

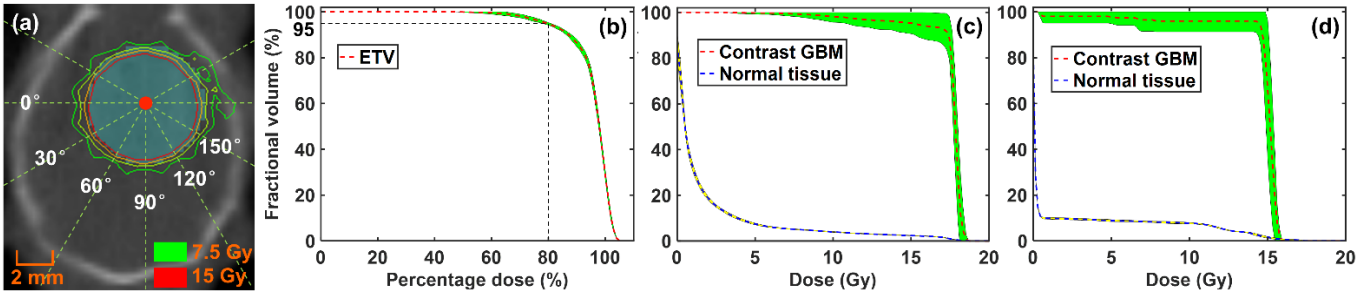

Figure S5. (a) Layout of the 6 arcs for ETV (2nd week)-based conformal irradiation; the angle and dash line show the couch angle. (b) Average ETV DVH with STD; average DVHs with STD of (c) 6-arc conformal and (d) single-DV-beam irradiation for contrast-delineated GBM and normal tissue. In the DVH plots, dash curves show the averages, and highlight areas show the range of STDs (n = 5, 2nd week). The upper STD is capped at 100% for tumor coverage.

Section 5. Workflow for BLT-CoM guided RT

Figure S6 shows the workflow of applying the BLT-CoM guided RT. Most of the work can be completed during the preparation phase. For animal irradiation, only BLT CoM is required to localize the tumor position. The pre-determined ETV is used to provide the target volume information.

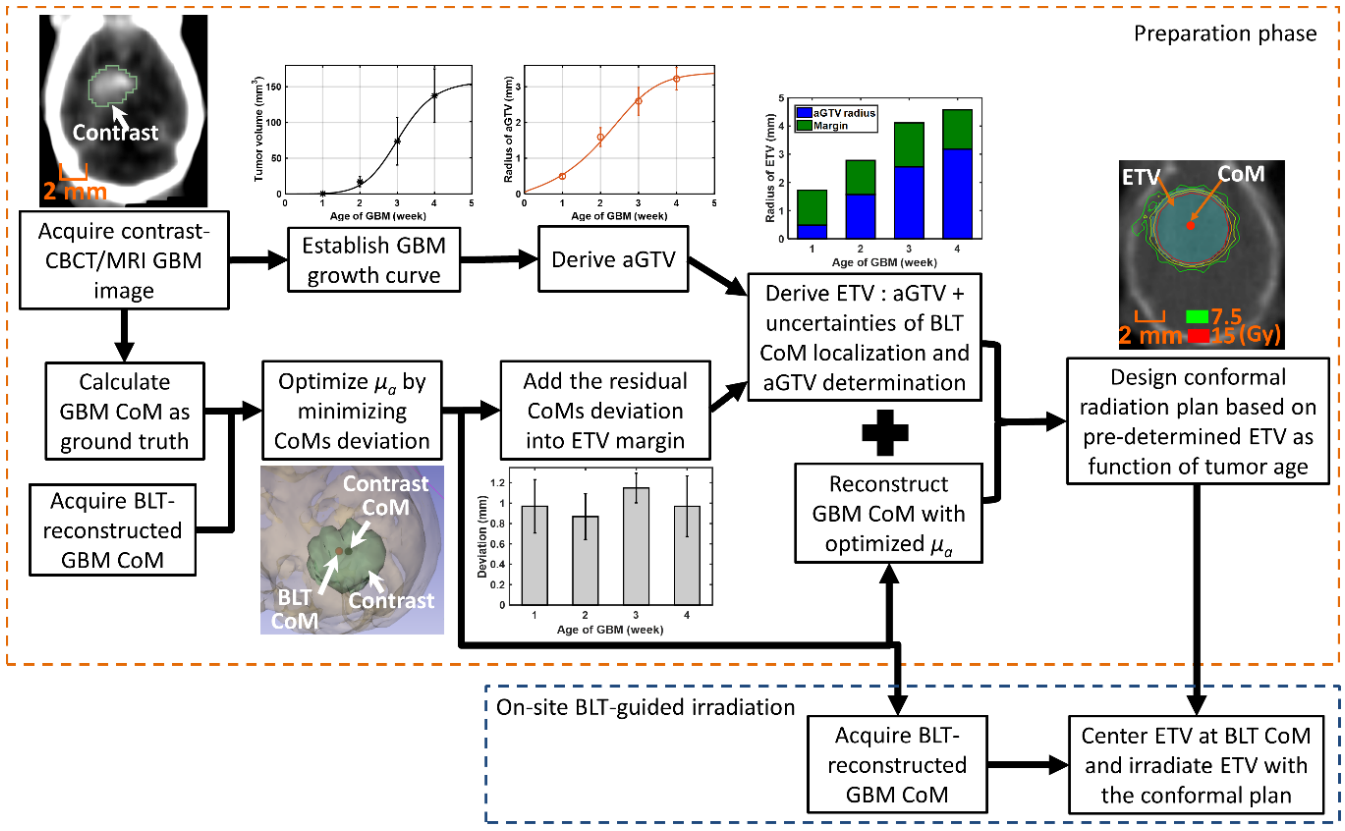

Figure S6. The workflow of BLT-CoM guided RT including the procedures from the premade treatment plan and the BLT-guided irradiation.

To facilitate the use of our data for the readers, we listed the numerical value of Figure 1, 3a, and 4a from the main article in Table 4. As we described in the main article, the μ_s' at 590, 610, 630 650 nm are 1.62, 1.56, 1.51, and 1.46 mm^{-1} respectively, used in our study. The refractive index of mouse brain was set as 1.4.

Table 4. Numerical value from Figure 1, 3a, and 4a

		1st week	2nd week	3rd week	4th week
Figure 1	GBM volume (mm^3)	0.49 ± 0.15	17.18 ± 7.02	73.56 ± 33.12	137.47 ± 37.36
	aGTV radius (mm)	0.48 ± 0.05	1.57 ± 0.26	2.55 ± 0.38	3.18 ± 0.31
Figure 3a	590 nm μ_a (mm^{-1})	0.4524 ± 0.0211	0.4673 ± 0.0168	0.4552 ± 0.0226	0.3702 ± 0.0730
	610 nm μ_a (mm^{-1})	0.0960 ± 0.0107	0.1017 ± 0.0031	0.1052 ± 0.0154	0.0809 ± 0.0070
	630 nm μ_a (mm^{-1})	0.0488 ± 0.0061	0.0520 ± 0.0019	0.0544 ± 0.0092	0.0414 ± 0.0034
	650 nm μ_a (mm^{-1})	0.0343 ± 0.0046	0.0367 ± 0.0015	0.0386 ± 0.0070	0.0292 ± 0.0024
Figure 4a	ETV radius (mm)	1.72	2.78	4.11	4.58

Section 6. Histologic and immunohistochemical staining

γ-H2AX assay reflects the presence of DNA double-strand breaks (21). We used the γ-H2AX assay to detect the γ-H2AX foci in 2D brain tissue section to identify the irradiation area introduced by the BLT-guided RT. To maintain morphologic features of tissue section (22), we utilized formalin-fixed, paraffin-embedded (FFPE) tissue preparation method to prepare the brain tissue. Mice (n = 4) were euthanized 60 min after BLT-guided irradiation. The brains were excised and fixed in 4% formaldehyde (Sigma-Aldrich, St. Louis, MO) for 24 hours. We approximated the center of GBM using the location of cell implementation, and cut each brain in half through the approximated center. Two brains were cut at coronal direction, and the other two were cut at transverse direction. We placed the *ex vivo* brain into tissue embedding cassette. The Johns Hopkins University Oncology Tissue Services (JHU OTS, http://tmalab.jhmi.edu/) further embedded the brains in paraffin, sectioned the paraffin-embedded brains into 5-μm slices, and placed the slices on charged microscope slides. Hematoxylin and eosin (H&E) was further performed by the JHU OTS. We chose the tissue section right next to the H&E staining section (5 μm apart) for the γ-H2AX and 4',6-diamidino-2-phenylindole (DAPI; Biotium, Fremont, CA) staining to label γ-H2AX foci and nuclei, respectively. For γ-H2AX staining, we deparaffinized and rehydrated the sections in sequence of "5 min Xylene (Fisher Chemical, Fisher Scientific, Fair Lawn, NJ), 5 min Xylene, 3 min 100% EtOH (Pharmco, Greenfield Global, Brookfield, CT), 3 min 100% EtOH, 3 min 95% EtOH, 3 min 95% EtOH, 3 min 70% EtOH, and 5 min distilled water". To retrieve all of antigens (including γ-H2AX and nonspecific binding sites) on the sections, we submerged the sections into 10-mM citrate buffer (Dako, Carpinteria, CA) at pH 6 and steamed them for 45 minutes at 95 °C. To block nonspecific binding sites for ensuring the binding of primary antibodies to γ-H2AX foci, we applied 4% bovine serum albumin (Sigma Life Science, Sigma-Aldrich, St. Louis, MO) to the sections for 30 min. After the preprocessing procedures, the sections were incubated with primary antibody, mouse anti-γ-H2AX antibody (1:500; Cell

Signaling Technology, Danvers, MA) overnight at 4 °C, followed by secondary antibody, Alexa-Fluoro 488 goat anti-mouse IgG (1:500; Life Technologies, Carlsbad, CA) for 1 hour at room temperature. After the γ-H2AX staining, the sections were counterstained with DAPI for 30 min. After dripping antifade medium Vectashield (Vector Laboratories, Burlington, ON, Canada) to the sections, we mounted coverslips onto the sections. The edges of coverslips were sealed with clear nail polish.

We used a high-content imager ImageXpress Micro (Molecular Devices, San Jose, CA) to acquire fluorescent images of the whole brain sections. Excitation/emission filters were set at 377/447 and 472/520 nm for nuclei and γ-H2AX foci labels, respectively. We chose an objective with 10-time magnification for the imager to acquire sub images (2.6 μm/pixel) of the tissue section, and then connected the sub images in sequence to generate an image of the whole tissue section.

Reference

1. Wong J, Armour E, Kazanzides P*, et al.* High-resolution, small animal radiation research platform with X-ray tomographic guidance capabilities. *Int. J. Radiat. Oncol. Biol. Phys.* 2008;71:1591-1599.

2. Matinfar M, Ford E, Iordachita I, *et al*. Image-guided small animal radiation research platform: Calibration of treatment beam alignment. *Phys. Med. Biol.* 2009;54:891-905.

3. Kuo C, Coquoz O, Troy TL, *et al*. Three-dimensional reconstruction of in vivo bioluminescent sources based on multispectral imaging. *J. Biomed. Opt.* 2007;12:024007.

4. Dehghani H, Davis SC, Jiang SD*, et al.* Spectrally resolved bioluminescence optical tomography. *Opt. Lett.* 2006;31:365-367.

5. Zhang B, Wang KK-H, Yu JJ*, et al.* Bioluminescence tomography-guided radiation therapy for preclinical research. *Int. J. Radiat. Oncol. Biol. Phys.* 2016;94:1144-1153.

6. Zeng J, See AP, Phallen J*, et al.* Anti-PD-1 blockade and stereotactic radiation produce long-term survival in mice with intracranial gliomas. *Int. J. Radiat. Oncol. Biol. Phys.* 2013;86:343-349.

7. Yang YD, Wang KKH, Eslami S*, et al.* Systematic calibration of an integrated X-ray and optical tomography system for preclinical radiation research. *Med. Phys.* 2015;42:1710-1720.

8. 3D Slicer. Available from: https://www.slicer.org/.

9. Kikinis R, Pieper SD, Vosburgh KG. 3D Slicer: A platform for subject-specific image analysis, visualization, and clinical support. In: Jolesz FA, ed. Intraoperative imaging and image-guided therapy. New York, NY: Springer New York, 2014;pp. 277-289.

10. Fedorov A, Beichel R, Kalpathy-Cramer J*, et al.* 3D Slicer as an image computing platform for the quantitative imaging network. *Magn. Reson. Imaging* 2012;30:1323-1341.

11. Jacques SL. Optical properties of biological tissues: A review. *Phys. Med. Biol.* 2013;58:R37-R61.

12. Zhao J, Ding HS, Hou XL, *et al*. In vivo determination of the optical properties of infant brain using frequency-domain near-infrared spectroscopy. *J. Biomed. Opt.* 2005;10:024028.

13. Ijichi S, Kusaka T, Isobe K*, et al.* Developmental changes of optical properties in neonates determined by near-infrared time-resolved spectroscopy. *Pediatr. Res.* 2005;58:568-573.

14. Abookasis D, Lay CC, Mathews MS*, et al.* Imaging cortical absorption, scattering, and hemodynamic response during ischemic stroke using spatially modulated near-infrared illumination. *J. Biomed. Opt.* 2009;14:024033.

15. O'Sullivan TD, Cerussi AE, Cuccia DJ, *et al*. Diffuse optical imaging using spatially and temporally modulated light. *J. Biomed. Opt.* 2012;17:071311.

16. Lin AJ, Koike MA, Green KN*, et al.* Spatial frequency domain imaging of intrinsic optical property contrast in a mouse model of Alzheimer's disease. *Ann. Biomed. Eng.* 2011;39:1349-1357.

17. Tabulated molar extinction coefficient for hemoglobin in water. Available from: http://omlc.org/spectra/hemoglobin/summary.html.

18. Pope RM, Fry ES. Absorption spectrum (380-700 nm) of pure water. II. Integrating cavity measurements. *Appl. Optics* 1997;36:8710-8723.

19. Jermyn M, Ghadyani H, Mastanduno MA, *et al.* Fast segmentation and high-quality three-dimensional volume mesh creation from medical images for diffuse optical tomography. *J. Biomed. Opt.* 2013;18:086007.

20. Dehghani H, Eames ME, Yalavarthy PK, *et al.* Near infrared optical tomography using NIRFAST: Algorithm for numerical model and image reconstruction. *Commun. Numer. Methods Eng.* 2009;25:711-732.

21. Kuo LJ, Yang LX. γ-H2AX - a novel biomarker for DNA double-strand breaks. *In Vivo* 2008;22:305-309.

22. Shi SR, Liu C, Pootrakul L*, et al.* Evaluation of the value of frozen tissue section used as "gold standard" for immunohistochemistry. *Am. J. Clin. Pathol.* 2008;129:358-366.